

Binary atomic silicon logic

Taleana Huff^{1,2*}, Hatem Labidi^{1,3}, Mohammad Rashidi¹, Lucian Livadaru², Thomas Diemel¹,
Roshan Achal^{1,2}, Wyatt Vine¹, Jason Pitters^{2,3} and Robert A. Wolkow^{1,2,3*}

It has been proposed that miniature circuitry will ultimately be crafted from single atoms. Despite many advances in the study of atoms and molecules on surfaces using scanning probe microscopes, challenges with patterning and limited thermal structural stability have remained. Here we demonstrate rudimentary circuit elements through the patterning of dangling bonds on a hydrogen-terminated silicon surface. Dangling bonds sequester electrons both spatially and energetically in the bulk bandgap, circumventing short-circuiting by the substrate. We deploy paired dangling bonds occupied by one moveable electron to form a binary electronic building block. Inspired by earlier quantum dot-based approaches, binary information is encoded in the electron position, allowing demonstration of a binary wire and an OR gate.

The prospect of atom-scale computing was initially indicated by molecular cascades in which sequentially toppling molecules were arranged in precise configurations to achieve binary logic functions¹. Many notable approaches towards molecular electronics^{2–6}, atomic electronics^{7–9} and quantum-dot-based electronics^{10–15} have also been explored. The quantum dot-based approaches^{16–20} are particularly attractive, as they could provide a low power yet fast basis²¹ to go beyond today's CMOS technology²². These approaches, however, require cryogenic temperatures to minimize the population of thermally excited states and achieve the desired functionality. Variability among quantum dots and sensitivity to uncontrolled fields are known to pose additional challenges²³. The prospect of partially circumventing these issues was reported in studies of silicon dangling bonds (DBs)—that is, unsatisfied bonds—on the otherwise hydrogen-terminated silicon surface (H-Si)^{15,24,25}.

Silicon DBs behave like quantum dots because they are zero-dimensional and exhibit three distinct charge states (positive, neutral, and negative) depending on their electron occupation (zero, one, or two electrons, respectively)^{26,27}. Consequently, DBs have two charge transition levels: the neutral to negative (0/−) transition and positive to neutral (+/0) transition. Crucially, because these DB energy levels lie within the bulk bandgap they are electronically isolated from the bulk^{27,28}. Silicon DBs approach the ultimate small size (single atom) for a quantum dot and therefore exhibit a larger energy level spacing, relaxing temperature requirements compared to larger conventional quantum dots¹³. Because all dots are identically composed of only one atom, inhomogeneities are limited to local environment variability, which in principle can be effectively eliminated.

H-Si was first identified as an attractive candidate for nanoscale patterning in 1996²⁵. DBs can be patterned at precise lattice locations, allowing their positions and spacing to be exactly defined^{25,29,30}. Only recently have capabilities reached the levels necessary to enable prototyping of structures on this surface. DBs can now be deterministically placed or erased (controlled H atom placement) using a scanned probe^{29,31,32}. Very recently, prospects for atom-scale fabrication have improved through the application of machine learning methods to automate some of the most challenging aspects of scanned probe atom-scale imaging and fabrication³³. It has also been established that structures made from DBs on the silicon surface are robust,

being stable against diffusion even at 200 °C, corresponding to a diffusion barrier of 1.4 eV (ref. ^{15,24,34}).

In this Article, we use these new tools and methods to characterize the charge distribution in DB ensembles, and extend earlier scanning tunnelling microscope (STM)^{15,28,35–41} and non-contact atomic force microscope (nc-AFM) studies^{27,31,42}. Pairs of closely spaced DBs have only a single negative net charge at low bias⁴². Addition of a nearby negative charge can sufficiently bias or 'tilt' the potential landscape of the DB pair so as to place the shared charge to one side of the pair or the other, corresponding to a well-defined binary zero or one. Thus, the pairs become the natural medium to encode binary information by localization of charge, as well as to perform logic operations. The ability to create^{25,29,30} and perfectly erase^{31,32} DBs is then used to fabricate and actuate rudimentary circuit elements. We employ the single-electron charge sensitivity of nc-AFM to probe the charge configuration and functionality of a fabricated binary wire and a logical OR gate (Supplementary Video 1).

Charge transitions in DBs

The nc-AFM images and spectra in Fig. 1a–e characterize the neutral and negative charge states of an isolated DB (corresponding STM details in Supplementary Fig. 1)²⁷. In frequency shift (Δf) images, recorded at constant height and selected fixed biases (Fig. 1a–c), the background H-Si appear as bright protrusions arranged in the 2×1 surface reconstruction of Si(100)⁴³ and the DB appears as a variably-dark depression, agreeing with previous AFM observation³¹. The charge transition of the DB is observed as a step-like feature at -350 mV in the blue Δf versus bias voltage spectrum ($\Delta f(V)$, Fig. 1d). Steps in $\Delta f(V)$ spectra taken above molecules and atoms are known to correspond to single-electron charge transitions^{27,44–47}, as changing the charge state of an entity underneath the tip changes the electrostatic force experienced by the tip, registering as a shift in resonance frequency.

The $\Delta f(V)$ spectrum of the DB can be explained qualitatively by considering its (0/−) charge transition level relative to the position of the tip's Fermi level as the bias voltage is swept, as detailed in other works^{26,27,41}. Isolated DBs on a highly n-type doped crystal, as studied here, are negatively charged at zero bias^{36,37,41}. When the tip's Fermi level is energetically above the (0/−) charge transition level of the DB (Fig. 1f), the DB is doubly occupied and therefore negative (region I in Fig. 1d). At the step in the $\Delta f(V)$ curve,

¹Department of Physics, University of Alberta, Edmonton, Alberta, Canada. ²Quantum Silicon, Inc., Edmonton, Alberta, Canada. ³Nanotechnology Research Centre, National Research Council Canada, Edmonton, Alberta, Canada. *e-mail: taleana@ualberta.ca; rwolkow@ualberta.ca

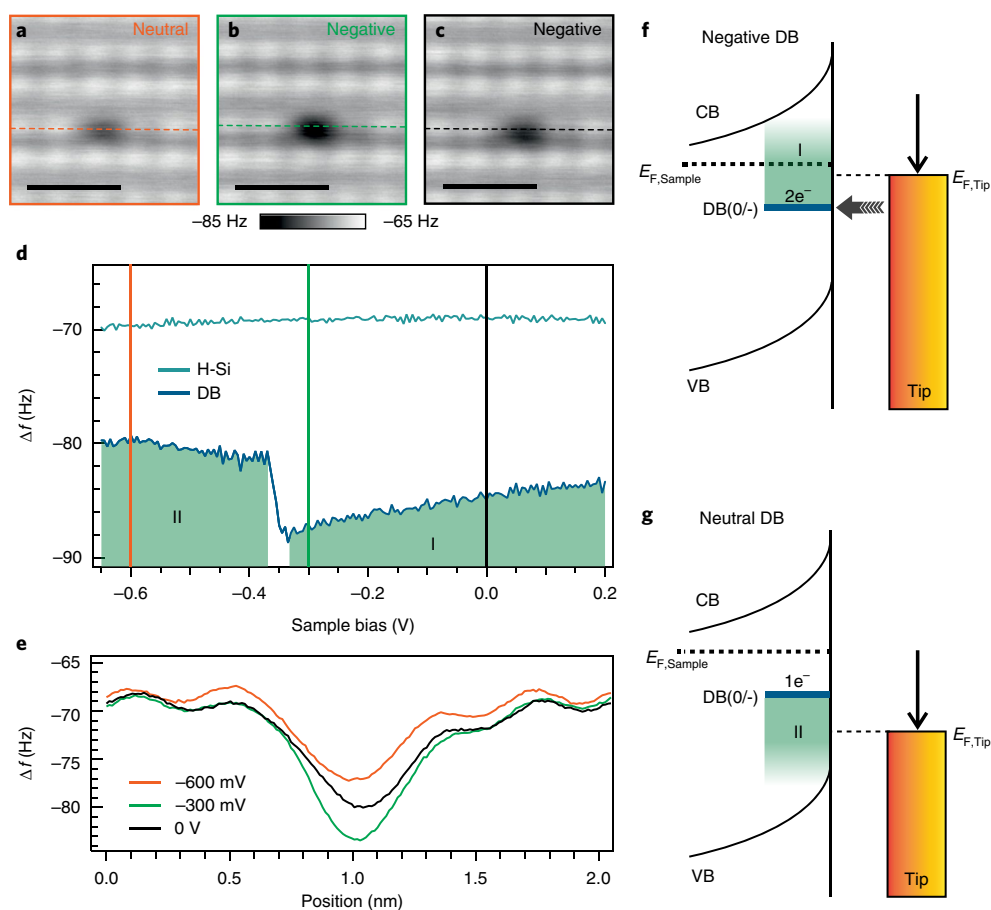


Fig. 1 | Probing charge state transitions of a DB. **a–c**, $2 \times 2 \text{ nm}^2$ constant height Δf images of an DB at different bias voltages ($z_{\text{rel}} = -350 \text{ pm}$ and $V = -600 \text{ mV}$ (**a**), $V = -300 \text{ mV}$ (**b**), $V = 0 \text{ V}$ (**c**); scale bars are 1 nm). **d**, Frequency shift versus sample bias ($\Delta f(V)$) measured above the hydrogen-terminated surface (teal curve) and the DB (blue curve) showing a charge transition step ($z_{\text{rel}} = -350 \text{ pm}$; see Supplementary Fig. 1 for STM details). Colour-coded vertical lines indicate the fixed sample bias at which the Δf images shown in **a–c** were taken. Green shaded regions I and II denote the negative and neutral charge state bias regions, respectively. **e**, Scan profiles extracted from **a–c** at the dashed lines as indicated. All scale bars are 1 nm . **f**, Qualitative band diagram of the tip–sample system when the DB is negatively charged. The tip Fermi level is above the negative to neutral charge transition level $\text{DB}(0/-)$, rendering it doubly occupied. **g**, Band diagram when the DB is neutral, showing the tip Fermi level below the DB’s charge transition level. Roman numerals in the green shaded regions in **f** and **g** correlate to the bias regions indicated in the DB’s $\Delta f(V)$ curve in **d**. VB, valence band. CB, conduction band.

the tip’s Fermi level becomes resonant with the $(0/-)$ charge transition level and the tip extracts an electron from the DB. Because the $(0/-)$ charge transition level of the DB at this bias voltage lies in the bandgap, the coupling to the tip is stronger than to the bulk and there is no efficient re-supply of electrons from the bulk to refill the DB. As a result, the DB is rendered neutral (Fig. 1g). Consequently, the step in $\Delta f(V)$ in Fig. 1d corresponds to the transition of the DB between its negative (right of the step, I) and neutral (left of the step, II) charge states²⁷. The associated difference in Δf between the hydrogen atoms (teal curve in Fig. 1d) and the DB at the marked fixed biases explains the contrast differences in the constant height nc-AFM scans of Fig. 1a–c. Profiles taken across the DBs in these images are shown in Fig. 1e and highlight the difference in Δf at the DB’s location. The magnitude of the attractive Δf shift indicates the charge state of the DB: a negatively charged DB (green and black line, Fig. 1e) appears darker and more attractive than a neutral one (orange line, Fig. 1e). Therefore, the contrast difference between DBs can be used as a direct indicator of their charge state.

Binary electronic building blocks

In Fig. 2, we build upon the established fundamental characteristics of an isolated DB to demonstrate the step-by-step fabrication

and characterization of a DB pair and the biasing of that pair by a negative charge positioned nearby. We began with an isolated DB (Fig. 2a–c). The isolated DB was created by applying a voltage pulse with the tip^{29,30} (see ‘Creating and erasing of DBs’ in Methods for details). The characterization of the isolated DB qualitatively resembles the observations presented in Fig. 1. To show that the second DB is identical to the first, the first DB was erased by controllably capping it with an H atom^{31,32}, so that the second DB could be studied in isolation. In this way it was ensured that the properties attributed to a DB pair are not due to a second DB of aberrant character. After erasure of the first DB, the new DB was created two lattice sites away (teal marker), and the characterization was repeated (Fig. 2d–f). The $\Delta f(V)$ spectra of both DBs in isolation (Fig. 2c,f) exhibit a charge transition step at -135 mV , confirming that they are identical.

By recreating the left DB (blue marker, Fig. 2h) a pair is formed^{15,42}. The $\Delta f(V)$ spectra (Fig. 2i) taken at each of the paired dots are identical. When compared with $\Delta f(V)$ spectra obtained above the isolated DBs (Fig. 2c,f), they exhibit a new step at 265 mV . The first step appears at the same energy as that of the isolated DBs (-135 mV). These observations can be understood by noting that below (more negative sample bias) -135 mV both DBs are neutral, between

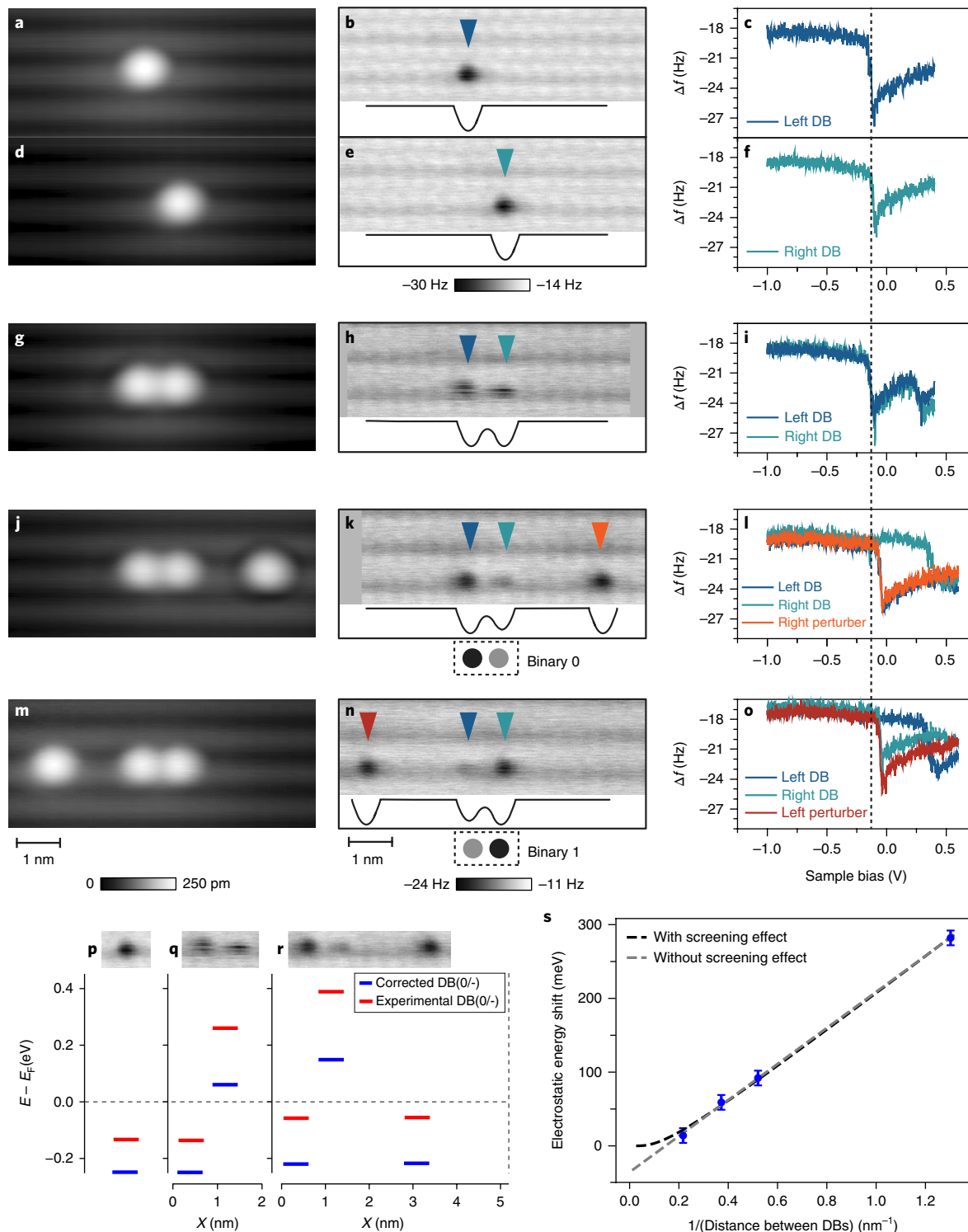


Fig. 2 | Biasing of DB structures. **a,d,g,j,m**, Filled state STM images of the isolated left (**a**), isolated right (**d**), coupled (**g**), biased right (**j**) and biased left (**m**) DB assemblies ($V = -1.8$ V, $I = 50$ pA). **b,e,h,k,n**, Corresponding frequency shift (Δf) images. $z_{\text{rel}} = -350$ pm for **b,e** and $z_{\text{rel}} = -300$ pm for **h,k** and **n** with $V = 0$ V. Qualitative potential energy well sketches are included at the bottom of each panel and the biased states in **k,n** also have their binary representation shown below. **c,f,i,l,o**, Corresponding colour-coded $\Delta f(V)$ spectra taken on top of the quantum dots in the frequency shift maps ($z_{\text{rel}} = -300$ pm). The charge transition onset for the isolated DB cases at -135 mV is marked with a vertical dashed line for reference. **p-r**, DB($0/-$) charge transition levels for the isolated, paired, and perturbed DBs, respectively. Red solid lines are the charge transition level experimentally measured. Blue lines are the corrected energy level in the absence of any tip-induced band bending. For **q**, two degenerate energy states exist. We illustrate the case of the electron localized on the left, but localization on the right also occurs. **s**, Corrected electrostatic energy shifts of the DB charge transition levels as a function of DB-to-DB distance for negatively charged DBs. Fits with and without screening factored in are plotted. Error bars reflect the read-out error of the electrostatic energy shift, estimated to be ± 10 mV.

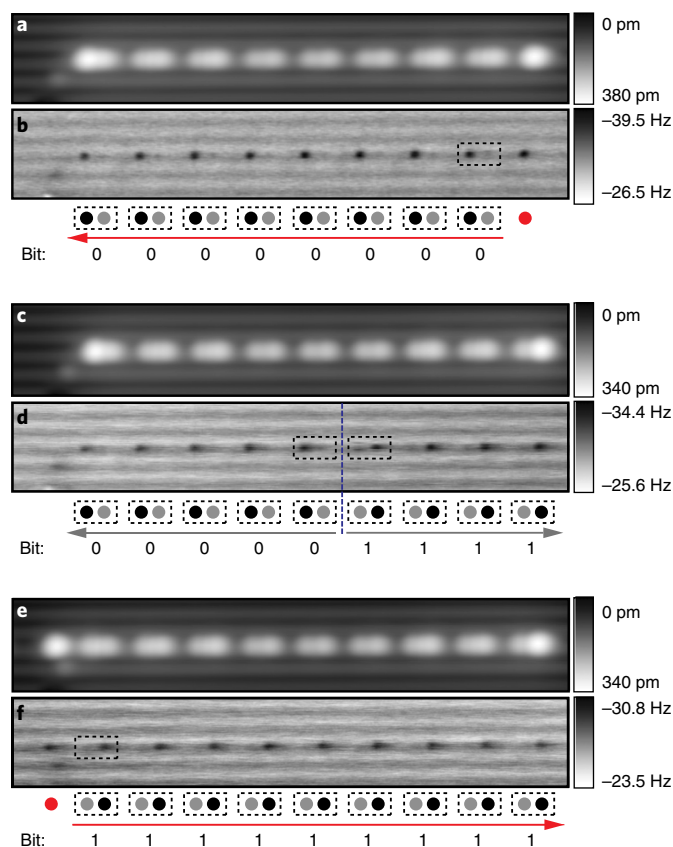


Fig. 3 | Information transmission through a DB binary wire. a, b Filled states STM image (a) and corresponding constant-height Δf image (b) of an eight-pair wire with a non-paired perturber DB (red circle) on the right. **c, d**, Symmetric nine-pair wire created from pairing up the red perturber DB in **b**. **d**, Constant-height Δf image of the nine-pair wire, with the symmetry-splitting plane marked by a dashed purple line. **e**, STM image of a nine-pair wire after adding a perturber DB (red circle in **f**) on the left. **f**, Constant-height Δf image showing the wire binary state under the field of the perturber (red). All STM images were taken at $V = -1.7$ V and $I = 50$ pA. All Δf images are $24 \text{ nm} \times 3 \text{ nm}$ in size and were taken at zero bias with a relative tip elevation of $z_{\text{rel}} = -330$ pm. Guides are placed below **b**, **d** and **f** to show the location and bit state of the pairs.

-135 mV and 265 mV only one DB is negatively charged, and above 265 mV both are negatively charged (see section ‘Pair of two DBs’ in Supplementary Information for more details). Therefore, under the imaging conditions of Fig. 2h (0 V), only one DB is negatively charged at a time, confirming the pair has one net negative charge, as reported in previous studies^{15,42}. Furthermore, the energetic position of the charge transition level of a paired DB is the same as that of an isolated DB, because the neutral character of its partner does not give rise to an electric field. In other words, a paired DB acts like an isolated DB for much of its $\Delta f(V)$ due to the electron localization on only one DB site. This observation of charge localization for a DB pair with a single intervening hydrogen atom is unexpected; previous explorations^{35,37,48,49} have reported that the individual quantum states of the two DBs should hybridize, resulting in molecular-like orbitals that would delocalize charge across the structure. This hybridization is inconsistent with the observations reported here, and we suggest two possible explanations. First, previous studies are based on STM experiments measured at higher energies and the hybridized states are believed to be related to excited states of the DB ensembles^{35,37}. At the low energies probed in our experiments, structures derived from DBs are possibly weakly coupled ground

states^{35,37}. Second, DBs are known to exhibit structural relaxation depending on their charge state^{35,37,50}. Density functional theory calculations have found an approximately 200 meV stabilization of negatively charged DBs, with the nuclear position of the host atom raised by 30 pm relative to that of the neutral state^{37,51,52}. Work has been reported³⁵ that has specifically examined DB pairs and structures made of DB pairs, with anisotropy in structural relaxation accounting for the reported device functionality. However, despite factoring in this structural relaxation, it was still found that charge was delocalized across the pairs, in contrast to our work. The full implications of lattice relaxation on the electronic structure of DB ensembles when combined with low-energy examination warrants future detailed investigation to explain these contradictory results.

Adding to the argument for localization, the streaky appearance of the DBs observed in Fig. 2h indicates that the localization fluctuates between a left and right state. The charge fluctuations we observe here are suspected to be the result of the tip, which, as it is scanning over the pair, occasionally gets too close due to noise in the oscillation amplitude set point, mechanically lifting the silicon atom beneath it and making the switch energetically favourable^{42,53}. This behaviour is due to short-range interactions between the tip and sample, and occurs with small tip–sample separations ($<400 \text{ pm}$ absolute tip height). The dividing line between the two regimes, one where charge states are imaged stably, and the other where the tip mechanically displaces the surface atoms, can be of the order of 20 pm (ref. 42), which is in line with amplitude set point noise estimates (see ‘Measurement system set-up’ in Methods). Here, the tip height was chosen to provide optimal contrast, while on average ensuring the tip was not interacting strongly. However, we acknowledge other explanations are possible to explain streakiness. The charge could access the conduction band and be repopulated from the bulk, the tip may aid as a tunnel ‘hopping’ island from left to right, electrons could tunnel from tip to DB, or electron–hole recombination could periodically destabilize the charge.

Next, a third DB is added five lattice sites away from the teal DB (orange marker, Fig. 2k). The Δf image now reveals a clear contrast between DBs in the pair (blue and teal marker, Fig. 2k). The $\Delta f(V)$ spectra taken above the three DBs (Fig. 2l) confirm that the blue and orange DBs are both negatively charged at 0 V where the Δf image was obtained, whereas the teal DB remains neutral. As the negatively charged DB appears darker than a neutral one in the Δf image; this demonstrates that the charge is biased to reside on the blue DB in the pair. We denote this pair’s charge configuration a binary zero and refer to the orange DB as an electrostatic perturber. By subsequently erasing the orange DB and adding a perturber (red marker) on the left side (five lattice sites away from the blue DB), we demonstrate that the opposite biased case can be achieved giving a binary one (Fig. 2m–o). Taken together, these observations show the binary character of the DB pair.

Some perturbation of DB spectra²⁷ and pairs of DBs³⁹ using local charges has been examined using STM methods before, as have charge state change dynamics in isolated DBs using an applied bias between tip and sample^{26,41}. These STM observations, however, were done under high-bias conditions. As observed in Fig. 2j,m the two perturbing DBs exhibit different characters in the STM image. This is a consequence of the perturbative tip field under high-bias conditions, which can ionize deep dopants⁵⁴, affecting the local potential landscape and in turn changing the STM contrast of the DB. However, at the low-bias conditions used in AFM imaging and spectroscopy, these effects are not present, permitting a uniform potential landscape, where all the DBs exhibit the same character. Additionally, free of these strong tip fields, AFM provides new information about these charge transitions that were previously hidden in the bandgap of the material, and allows us to extract information about the DB interactions from shifts in the AFM spectroscopy.

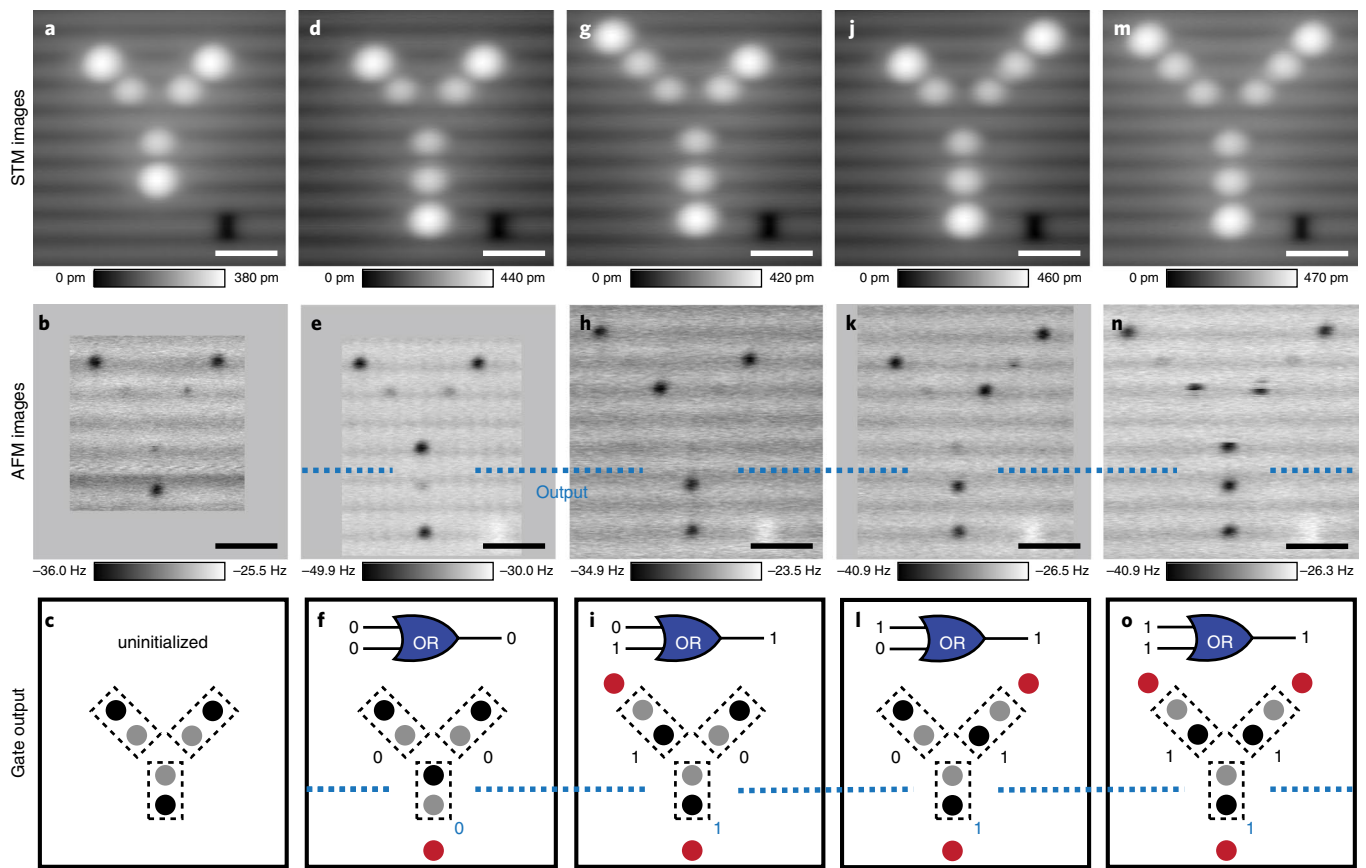


Fig. 4 | OR gate constructed of dangling bonds. **a,d,g,j,m**, Constant-current filled state STM images ($V = -1.8$ V, $I = 50$ pA) of the OR gate in various actuation states. **b,e,h,k,n**, Corresponding constant-height Δf images ($V = 0$ V, $z_{\text{rel}} = -350$ pm) of the gate, showing electron locations as the dark depressions, with the output marked in blue. **c,f,i,l,o**, Models of the gate. **c**, Three pairs constituting the uninitialized OR gate. **f**, Initialized gate with added red perturber below to satisfy the first row of an OR gate truth table, as indicated by the gate symbol. **i,l,o**, Models for the remaining OR gate truth states. All the models of the gates correspond to the experimental data shown vertically above them. Dashed boxes and numbers indicate the pairs and their binary state, and the single red perturbers are stand-ins for connecting wires or connections to other gates and structures. Scale bars are 2 nm.

We note here that for both tipped cases, the charge transition of the negative DBs are shifted to -50 mV from -135 mV for an isolated DB (marked by the dashed vertical line). This is due to the two negative DBs being in close enough proximity to interact and mutually shift their charge transition levels to a less negative value—that is, they are close enough to slightly perturb each other—without one or the other being ionized as in the paired case from Fig. 2h. The neutral DB exerts no effect on the negative DBs. In contrast, the presence of two negatively charged DBs next to the neutral DB strongly shifts its charge transition to 395 mV (Supplementary Fig. 2f,i).

The experiments in Fig. 2 can be explained with simple electrostatics and by assuming that negative DBs act as point charges. The red lines in Fig. 2p–r depict the measured energies of the DBs' ($0/-$) charge transition levels for the isolated, paired, and biased cases, respectively, extracted from the $\Delta f(V)$ spectra of Fig. 2. The tip-induced band bending (see the section 'Details on tip-induced band bending' in Supplementary Information) was calculated and factored in to obtain the corrected DB($0/-$) charge transition levels in the absence of the tip (solid blue lines, Fig. 2p–r). The ($0/-$) charge transition level of the corrected isolated DB (Fig. 2p) is 0.23 eV below the Fermi level. This is in agreement with ($0/-$) charge transition energies for Si(100)/SiO₂ interface dangling bonds (P_{b0} centres)⁵⁵ where a value of 0.27 ± 0.1 eV was reported. We note that ab initio calculations report notably lower values for the negative DB state than our obtained value^{28,37,48,56,57}.

Figure 2q highlights that closely spaced DB pairs have a single negative charge on one side or the other. As a result of Coulomb repulsion only the ($0/-$) charge transition level of one of the DBs is below the Fermi level and that of the other DB is lifted above the Fermi level, rendering it neutral. However, the pair system is degenerate. We have illustrated the case where the right DB is neutral and the left DB is negative, but note that the opposite can occur, as evidenced by the streakiness discussed earlier. However, whichever side it chooses in the pair, it appears to stay localized until an outside force changes it.

Adding the perturber DB (Fig. 2r) is such an example, and fixes the charge on one side. From the corrected DB($0/-$) charge transition levels we can extract the energy shift as a function of its separation from another negatively charged DB (Fig. 2s). We fit the data with the screened Coulomb energy equation³⁸,

$$U(r) = \frac{e}{4\pi\epsilon_0\epsilon r} e^{-r/L_{\text{TF}}}$$

where e is the elementary charge, ϵ_0 is the permittivity of free space, ϵ is effective dielectric constant at the surface, r is the distance between DBs and L_{TF} is the Thomas-Fermi screening length. From the fit (black dashed line, Fig. 2s), ϵ and L_{TF} were extracted to be 5.6 and 5 nm, respectively. We note that without factoring in the screening effect, the fit results in a physically invalid negative offset energy (grey dashed line, Fig. 2s).

Figure 2 summarizes the underlying principles of our approach, where we define the two biased configurations of the pair as two binary states. By creating larger ensembles, more complex functionality can be achieved. We now provide two additional examples: a binary wire and a logical OR gate.

Binary wire

Figure 3 demonstrates that the electrostatically determined binary state of a DB pair can be extended over a line formed of many paired DBs. Figure 3a shows an STM image of a wire constructed from eight pairs, with a lone perturber on its right. The constant-height Δf image below (Fig. 3b) shows that the perturber (red marker) tips the eight pairs to the left. In Fig. 3c, an additional DB is patterned next to the red DB so that it forms a ninth pair. The Δf image (Fig. 3d) demonstrates that such an ensemble, lacking a perturbing electrostatic input, becomes self-polarized, with the pairs on either side of its midpoint adopting opposite polarizations (division indicated by the purple dashed line). In Fig. 3e,f a new perturber (red marker) is patterned on the left side of the ensemble, reversing the state. The sequence of images in Fig. 3 demonstrates the basis for a binary wire. Because we are limited at this point to negative charges as inputs, we are restricted to demonstrating the two states of the wire by pushing with charges from an input placed at one end of the line or the other.

Logical OR gate

Figure 4 shows a logical OR gate can also be achieved through a two-dimensional arrangement of DBs. In its uninitialized form the gate consists of three pairs arranged in a Y shape (Fig. 4a–c). We define the two upper branches as the gate's inputs, and the lower branch as the gate's output (the dashed boxes depict the three pairs defining the gate). In the absence of perturbers, the mutual electrostatic repulsion among the electrons within the pairs causes the electrons to localize to the outermost DBs (Δf image in Fig. 4b). The addition of a perturber below the output branch (Fig. 4d–f) forces the output electron towards the centre of the gate structure and initializes the gate (Fig. 4e,f). The perturber (red dot in Fig. 4f) allows the first row of the truth table for an OR gate to be realized (see Supplementary Table 1). The inputs can now be toggled with perturbers placed at either of the input branches (Fig. 4g–i and j–l) or both (Fig. 4m–o), with the effect being that the electrostatic push from the perturber below the output branch is overcome, enforcing an output of 1 at the designated output. Together these configurations satisfy the remaining rows of the truth table. The charge fluctuations observed in Fig. 4n are suspected to be the result of the tip scanning over the structure (compare discussion of Fig. 2h).

It is anticipated that more complex functionality can be achieved by linking multiple gates together with the binary wires presented in Fig. 3. Such a theoretical design is shown in Supplementary Fig. 6, with two interconnected OR gates linked by a single-bit binary wire. There, the bottom OR gate has an initializing electrostatic perturber and sets the correct state for the whole ensemble, allowing more complex operation. This design was simulated using SimAnneal, a ground-state electron configuration testing package⁵⁹ (details in section 'SimAnneal' in Supplementary Information). Through patterning of bits in different arrangements and with varied coupling strengths, other gate designs are foreseen (as shown in ref. 59). The perturber inputs used in all tested and theorized logic designs are intended to be replaced in future implementations with binary wires or metallic leads⁶⁰.

Conclusions

We have demonstrated a set of rudimentary binary circuit elements formed of silicon DB gap states. Precise atomic fabrication allowed the reproducible patterning of bits formed of DB pairs holding only one negative charge. Electrostatic perturbers were used to tip the potential energy landscape of the pairs and thus set the binary

state of the bits, mapped as the electrons' spatial arrangements. Assemblies of bits formed a binary wire and a logical OR gate.

We anticipate that, with our approach, connections to external circuitry can be made through atomic wire leads⁶⁰ with readout transduced by single-electron transistors (refs. 61–63) or quantum point contacts^{17,64}. A wafer bonding approach^{65,66} could also be used to permanently encapsulate and environmentally protect the circuitry, allowing it to be removed from the fabrication environment and transported. Although there are indications that field-controlled computing approaches like ours might operate in a very low power and yet ultra-fast regime^{12,14,20}, detailed studies of power consumption and speed of operation remain to be done. There have also been previous indications that the polarization of a bit persists at room temperature^{13,15,39}, but, because effects such as excitation of electrons to the conduction band^{41,48} could disrupt logic functions, further testing is required to understand whether room-temperature operation is feasible. Many challenges remain, but recent advances towards exact and automated DB patterning suggest that increased complexity could be possible^{29,31,33}.

Methods

Measurement system set-up. Experiments were carried out using a commercial (Scienta Omicron) qPlus AFM system operating at 4.5 K. Nanonis control electronics and software were used for both STM and AFM data acquisition. For all constant-height frequency shift images and the bias-dependent spectroscopy, $z_{\text{rel}} = 0$ pm corresponds to the relative tip elevation defined by the STM imaging set points on the site of hydrogen-terminated silicon $I = 50$ pA and $V = -1.8$ V. The tuning fork had a resonance frequency of 32.8834450 kHz, with a quality factor of 40,000. The tuning fork was driven with an oscillation amplitude of 50 pm and recorded to be at 50 ± 20 pm. To minimize drift during AFM image acquisition, the tip was left to settle for 12 hours after approach to allow piezo scanner stabilization. All STM and AFM images are raw data. The tip height has to be carefully chosen for every tip-sample combination to obtain optimal contrast, while ensuring the tip does not mechanically displace the surface atoms due to covalent or van der Waals interactions^{42,53}. The transition region where the regimes blend is approximately 20–30 pm wide and is centred at approximately $z_{\text{rel}} = -300$ pm from the specified STM set point. This approximate z_{rel} will change slightly for different tip-sample combinations.

Sample preparation. Highly arsenic-doped ($\sim 1.5 \times 10^{19}$ atom cm^{-3}) Si(100) was used. Sample preparation involved degassing at ~ 600 °C for 12 hours in ultra-high-vacuum (UHV), followed by a series of resistive flash anneals reaching 1,250 °C to remove oxide, and finally holding the Si substrate at 330 °C for two minutes while molecular hydrogen (pressure = 10^{-6} torr) was cracked on a 1,600 °C tungsten filament. The series of resistive flash anneals has been shown to reduce surface dopant density, creating a depletion region ~ 70 nm below the sample surface with a donor concentration $\sim 10^{18}$ atom cm^{-3} (refs. 36,67).

Tip preparation. A focused ion beam (FIB) was used to cut a micro-tip from electrochemically etched 50 μm polycrystalline tungsten wire, then weld it to the end of a qPlus-style AFM sensor⁶⁸. UHV preparation involved having the oxide layer removed by electron bombardment heating treatments, followed by field evaporation to clean the apex in a field ion microscope (FIM)⁶⁹. Further sharpening was conducted using a FIM nitrogen etching process to obtain the smallest possible tip radius of curvature⁶⁹. Final in situ tip processing was done through creation of a bare silicon patch through tip-induced hydrogen desorption, followed by gentle controlled contacts with the tip on the reactive patch⁴³.

Creating and erasing DBs. To create a DB, a sharp artefact-free tip is positioned on top of a surface hydrogen atom at 1.3 V and 50 pA, and pulses of 2.0–2.5 V for 10 ms are applied until the hydrogen is removed^{25,29,30}. Some percentage of the time, the removed single hydrogen atom ends up functionalizing the tip apex. This functionalized tip can be positioned over a DB and mechanically brought towards it to induce a covalent bond and passivate it^{31,32}.

Data availability

The data that support the plots within this paper and other findings of this study are available from the corresponding author upon reasonable request.

Received: 19 June 2018; Accepted: 26 November 2018;
Published online: 13 December 2018

References

- Heinrich, A. J., Lutz, C. P., Gupta, J. A. & Eigler, D. M. Molecule cascades. *Science* **298**, 1381–1387 (2002).

2. de Silva, A. P., Uchiyama, S., Vance, T. P. & Wannalser, B. A supramolecular chemistry basis for molecular logic and computation. *Coord. Chem. Rev.* **251**, 1623–1632 (2007).
3. Soe, W. H. et al. Demonstration of a NOR logic gate using a single molecule and two surface gold atoms to encode the logical input. *Phys. Rev. B* **83**, 155443 (2011).
4. Collier, C. P. et al. Electronically configurable molecular-based logic gates. *Science* **285**, 391–394 (1999).
5. de Silva, A. P. & Uchiyama, S. Molecular logic and computing. *Nat. Nanotech.* **2**, 399–410 (2007).
6. Joachim, C., Gimzewski, J. K. & Aviram, A. Electronics using hybrid-molecular and mono-molecular devices. *Nature* **408**, 541–548 (2000).
7. Khajetoorians, A. A., Wiebe, J., Chilian, B. & Wiesendanger, R. Realizing all-spin-based logic operations atom by atom. *Science* **332**, 1062–1064 (2011).
8. Fresch, B., Bocquel, J., Rogge, S., Levine, R. D. & Remacle, F. A probabilistic finite state logic machine realized experimentally on a single dopant atom. *Nano. Lett.* **17**, 1846–1852 (2017).
9. Kolmer, M. & Joachim, C. *On-surface Atomic Wires and Logic Gates* (Springer International Publishing, Cham, 2014).
10. Amlani, I. et al. Digital logic gate using quantum-dot cellular automata. *Science* **284**, 289–291 (1999).
11. Imre, A. et al. Majority logic gate for magnetic quantum-dot cellular automata. *Science* **311**, 205–208 (2006).
12. Lent, C. S. & Tougaw, P. D. A device architecture for computing with quantum dots. *Proc. IEEE* **85**, 541–557 (1997).
13. Wolkow, R. A. et al. in *Field-Coupled Nanocomputing: Paradigms, Progress, and Perspectives* (eds Anderson, N. G. & Bhanja, S.) 33–58 (Springer-Verlag, Berlin Heidelberg, 2014).
14. Orlov, A. O., Amlani, I., Bernstein, G. H., Lent, C. S. & Snider, G. L. Realization of a functional cell for quantum-dot cellular automata. *Science* **277**, 928–930 (1997).
15. Haider, M. B. et al. Controlled coupling and occupation of silicon atomic quantum dots at room temperature. *Phys. Rev. Lett.* **102**, 046805 (2009).
16. Gorman, J., Hasko, D. G. & Williams, D. A. Charge-qubit operation of an isolated double quantum dot. *Phys. Rev. Lett.* **95**, 090502 (2005).
17. Kim, D. et al. Quantum control and process tomography of a semiconductor quantum dot hybrid qubit. *Nature* **511**, 70–74 (2014).
18. Schedelbeck, G., Wegscheider, W., Bichler, M. & Abstreiter, G. Coupled quantum dots fabricated by cleaved edge overgrowth: from artificial atoms to molecules. *Science* **278**, 1792–1795 (1997).
19. Bayer, M. et al. Coupling and entangling of quantum states in quantum dot molecules. *Science* **291**, 451–453 (2001).
20. Lent, C. S., Tougaw, P. D., Porod, W. & Bernstein, G. H. Quantum cellular automata. *Nanotechnology* **4**, 49–57 (1993).
21. Landauer, R. Minimal energy requirements in communication. *Science* **272**, 1914–1918 (1996).
22. Mathur, N. Beyond the silicon roadmap. *Nature* **419**, 573–575 (2002).
23. Shibata, K., Yuan, H., Iwasa, Y. & Hirakawa, K. Large modulation of zero-dimensional electronic states in quantum dots by electric-double-layer gating. *Nat. Commun.* **4**, 2664 (2013).
24. McEllistrem, M., Allgeier, M. & Boland, J. J. Dangling bond dynamics on the silicon (100)-2×1 surface: dissociation, diffusion, and recombination. *Science* **279**, 545–548 (1998).
25. Lyding, J. W., Shen, T. C., Abeln, G. C., Wang, C. & Tucker, J. R. Nanoscale patterning and selective chemistry of silicon surfaces by ultrahigh-vacuum scanning tunneling microscopy. *Nanotechnology* **7**, 128–133 (1996).
26. Taucer, M. et al. Single-electron dynamics of an atomic silicon quantum dot on the H-Si(100)-(2×1) surface. *Phys. Rev. Lett.* **112**, 256801 (2014).
27. Rashidi, M. et al. Resolving and tuning carrier capture rates at a single silicon atom gap state. *ACS Nano* **11**, 11732–11738 (2017).
28. Scherpelz, P. & Galli, G. Optimizing surface defects for atomic-scale electronics: Si dangling bonds. *Phys. Rev. Mater.* **1**, 021602 (2017).
29. Achal, R. et al. Lithography for robust and editable atomic-scale silicon devices and memories. *Nat. Commun.* **9**, 2778 (2018).
30. Shen, T. C. et al. Atomic-scale desorption through electronic and vibrational excitation mechanisms. *Science* **268**, 1590–1592 (1995).
31. Huff, T. R. et al. Atomic white-out: enabling atomic circuitry through mechanically induced bonding of single hydrogen atoms to a silicon surface. *ACS Nano* **11**, 8636–8642 (2017).
32. Pavliček, N., Majzik, Z., Meyer, G. & Gross, L. Tip-induced passivation of dangling bonds on hydrogenated Si(100)-2×1. *Appl. Phys. Lett.* **111**, 053104 (2017).
33. Rashidi, M. & Wolkow, R. A. Autonomous scanning probe microscopy in situ conditioning through machine learning. *ACS Nano* **12**, 5185–5189 (2018).
34. Schwalb, C. H., Dürr, M. & Höfer, U. High-temperature investigation of intradimer diffusion of hydrogen on Si(001). *Phys. Rev. B* **82**, 193412 (2010).
35. Yengui, M., Duverger, E., Sonnet, P. & Riedel, D. A two-dimensional ON/OFF switching device based on anisotropic interactions of atomic quantum dots on Si(100):H. *Nat. Commun.* **8**, 2211 (2017).
36. Labidi, H. et al. Scanning tunneling spectroscopy reveals a silicon dangling bond charge state transition. *New J. Phys.* **17**, 073023 (2015).
37. Schofield, S. R. et al. Quantum engineering at the silicon surface using dangling bonds. *Nat. Commun.* **4**, 1649 (2013).
38. Kolmer, M. et al. Atomic scale fabrication of dangling bond structures on hydrogen passivated Si(001) wafers processed and nanopackaged in a clean room environment. *Appl. Surf. Sci.* **288**, 83–89 (2014).
39. Pitters, J. L., Livadaru, L., Haider, M. B. & Wolkow, R. A. Tunnel coupled dangling bond structures on hydrogen terminated silicon surfaces. *J. Chem. Phys.* **134**, 064712 (2011).
40. Hitosugi, T. et al. Jahn–Teller distortion in dangling-bond linear chains fabricated on a hydrogen-terminated Si(100)-2×1 Surface. *Phys. Rev. Lett.* **82**, 4034–4037 (1999).
41. Livadaru, L., Pitters, J., Taucer, M. & Wolkow, R. A. Theory of nonequilibrium single-electron dynamics in STM imaging of dangling bonds on a hydrogenated silicon surface. *Phys. Rev. B* **84**, 205416 (2011).
42. Rashidi, M. et al. Initiating and monitoring the evolution of single electrons within atom-defined structures. *Phys. Rev. Lett.* **121**, 166801 (2018).
43. Labidi, H. et al. Indications of chemical bond contrast in AFM images of a hydrogen-terminated silicon surface. *Nat. Commun.* **8**, 14222 (2017).
44. Bussmann, E. & Williams, C. C. Single-electron tunneling force spectroscopy of an individual electronic state in a nonconducting surface. *Appl. Phys. Lett.* **88**, 263108 (2006).
45. Steurer, W. et al. Manipulation of the charge state of single Au atoms on insulating multilayer films. *Phys. Rev. Lett.* **114**, 036801 (2015).
46. Stomp, R. et al. Detection of single-electron charging in an individual InAs quantum dot by noncontact atomic-force microscopy. *Phys. Rev. Lett.* **94**, 056802 (2005).
47. Wagner, C. et al. Scanning quantum dot microscopy. *Phys. Rev. Lett.* **115**, 026101 (2015).
48. Livadaru, L. et al. Dangling-bond charge qubit on a silicon surface. *New J. Phys.* **12**, 83018 (2010).
49. Shaterzadeh-Yazdi, Z., Sanders, B. C. & DiLabio, G. A. Ab initio characterization of coupling strength for all types of dangling-bond pairs on the hydrogen-terminated Si(100)-2×1 surface. *J. Chem. Phys.* **148**, 154701 (2018).
50. Bellec, A. et al. Reversible charge storage in a single silicon atom. *Phys. Rev. B* **88**, 241406 (2013).
51. Kawai, H., Neucheva, O., Yap, T. L., Joachim, C. & Saeyns, M. Electronic characterization of a single dangling bond on n- and p-type Si(001)-(2×1):H. *Surf. Sci.* **645**, 88–92 (2016).
52. Northrup, J. E. Effective correlation energy of a Si dangling bond calculated with the local-spin-density approximation. *Phys. Rev. B* **40**, 5875–5878 (1989).
53. Sweetman, A. et al. Toggling bistable atoms via mechanical switching of bond angle. *Phys. Rev. Lett.* **106**, 136101 (2011).
54. Rashidi, M. et al. Time-resolved single dopant charge dynamics in silicon. *Nat. Commun.* **7**, 13258 (2016).
55. Gerardi, G. J., Poindexter, E. H., Caplan, P. J. & Johnson, N. M. Interface traps and Pb centers in oxidized (100) silicon wafers. *Appl. Phys. Lett.* **49**, 348–350 (1986).
56. Blomquist, T. & Kirzenow, G. Controlling the charge of a specific surface atom by the addition of a non-site-specific single impurity in a Si nanocrystal. *Nano. Lett.* **6**, 61–65 (2006).
57. Bellec, A. et al. Electronic properties of the n-doped hydrogenated silicon (100) surface and dehydrogenated structures at 5 K. *Phys. Rev. B* **80**, 245434 (2009).
58. Schubert, E. F. *Doping in III-V Semiconductors* (Cambridge Univ. Press, Cambridge, 2015).
59. Ng, S. et al. SiQAD: A design and simulation tool for atomic silicon quantum dot circuits. Preprint at <https://arxiv.org/abs/1808.04916> (2018).
60. Engelund, M. et al. Search for a metallic dangling-bond wire on n-doped H-passivated semiconductor surfaces. *J. Phys. Chem. C* **120**, 20303–20309 (2016).
61. Barthel, C. et al. Fast sensing of double-dot charge arrangement and spin state with a radio-frequency sensor quantum dot. *Phys. Rev. B* **81**, 161308 (2010).
62. Fuechle, M. et al. A single-atom transistor. *Nat. Nanotech.* **7**, 242–246 (2012).
63. Prager, A. A., Orlov, A. O. & Snider, G. L. Integration of CMOS, single electron transistors, and quantum dot cellular automata. *2009 IEEE Nanotechnology Materials and Devices Conference* 54–58 (IEEE, 2009); <https://doi.org/10.1109/NMDC.2009.5167548>
64. Goan, H. S., Milburn, G. J., Wiseman, H. M. & Bi Sun, H. Continuous quantum measurement of two coupled quantum dots using a point contact: a quantum trajectory approach. *Phys. Rev. B* **63**, 125326 (2001).
65. Sordes D. et al. in *On-surface Atomic Wires and Logic Gates* (eds Kolmer, M. & Joachim, C.) 25–51 (Springer International Publishing, Cham, 2014).
66. Eng, K., McFarland, R. N. & Kane, B. E. High mobility two-dimensional electron system on hydrogen-passivated silicon(111) surfaces. *Appl. Phys. Lett.* **87**, 52106 (2005).

67. Pitters, J. L., Piva, P. G. & Wolkow, R. A. Dopant depletion in the near surface region of thermally prepared silicon (100) in UHV. *J. Vac. Sci. Technol. B* **30**, 21806 (2012).
68. Labidi, H. et al. New fabrication technique for highly sensitive qPlus sensor with well-defined spring constant. *Ultramicroscopy* **158**, 33–37 (2015).
69. Rezeq, M., Pitters, J. & Wolkow, R. Tungsten nanotip fabrication by spatially controlled field-assisted reaction with nitrogen. *J. Chem. Phys.* **124**, 204716 (2006).

Acknowledgements

We thank M. Cloutier, D. Vick and M. Salomons for their technical expertise. We thank NRC, NSERC, QSi, Alberta Innovates, and Compute Canada for financial support. We thank F. Giessibl for providing us with the tuning forks for building the qPlus sensors. We thank K. Gordon for valuable suggestions and discussions. We thank B. Hesson for making and rendering the 3D animated Supplementary Video.

Author contributions

T.H., H.L., M.R., T.D., R.A. and W.V. designed and performed the experiments and analysed the data. T.H., R.A.W., T.D., L.L., W.V. and M.R. co-wrote the paper. L.L. and

M.R. performed the theoretical modelling. J.P. and R.A. contributed to the interpretation and discussion of the results. R.A.W. conceived of and supervised the project. All authors discussed the results and commented on the manuscript.

Competing interests

The authors declare competing financial interests: a patent has been filed on this subject. Some of the authors are affiliated with Quantum Silicon Inc. (QSi). QSi is seeking to commercialize atomic silicon quantum dot-based technologies.

Additional information

Supplementary information is available for this paper at <https://doi.org/10.1038/s41928-018-0180-3>.

Reprints and permissions information is available at www.nature.com/reprints.

Correspondence and requests for materials should be addressed to T.H. or R.A.W.

Publisher's note: Springer Nature remains neutral with regard to jurisdictional claims in published maps and institutional affiliations.

© The Author(s), under exclusive licence to Springer Nature Limited 2018

In the format provided by the authors and unedited.

Binary atomic silicon logic

Taleana Huff ^{1,2*}, **Hatem Labidi**^{1,3}, **Mohammad Rashidi** ¹, **Lucian Livadaru**², **Thomas Dienel** ¹,
Roshan Achal^{1,2}, **Wyatt Vine**¹, **Jason Pitters**^{2,3} and **Robert A. Wolkow** ^{1,2,3*}

¹Department of Physics, University of Alberta, Edmonton, Alberta, Canada. ²Quantum Silicon, Inc., Edmonton, Alberta, Canada. ³Nanotechnology Research Centre, National Research Council Canada, Edmonton, Alberta, Canada. *e-mail: taleana@ualberta.ca; rwalkow@ualberta.ca

Table of contents

- Further details on $\Delta f(V)$ Spectroscopy
 - Pair of Two DBs
 - One DB Perturbing a Pair
 - Symmetrically Perturbed Pair of DBs
- Truth Table of an OR Gate
- Sim Anneal
- Details on Tip-induced Band Bending
- Supplementary References
- Supplementary Figures

Further details on $\Delta f(V)$ Spectroscopy

Supplementary Figure 2 reproduces the bias-dependent frequency shift spectra shown in Fig. 2 of the main text, but with a vertical offset. The vertical offset allows clear discernment of all features and shifts in the graph for the DB pair (Supplementary Figure 2a,b,c), the pair biased to the left (Supplementary Figure 2d,e,f), the pair biased to the right (Supplementary Figure 2g,h,i), and the symmetrically biased pair (Supplementary Figure 2j,k,l). The error to read out the corresponding shifts of the charge transition energies are estimated to be ± 10 mV.

Pair of two DBs: For both DBs, the charge transition step is observed at -135 mV, identical to the case of the individual DBs (Fig. 2c,f in the main text). The reason is that only one DB of the pair can harbour an electron in this voltage range (-135 to 265 mV) and the remaining neutral DB does not exert an electric field on its neighbouring DB. Furthermore, once the negative charge is localized on one DB, its neighbouring DB has its negative to neutral charge transition level instantaneously shifted upward by the Coulomb field of its charged neighbour above the Fermi-level of the sample. This is qualitatively depicted in Supplementary Figure 3b. Assuming the blue DB is negative in this example case, as the sample bias is increased further past the second step (≥ 265 mV), the Fermi level of the tip is raised above the charge transition level DB(0/-) of the teal DB, which captures an electron and becomes negative too (Supplementary Figure 3c). This corresponds to both DBs being negative, and to the second step in the $\Delta f(V)$ spectrum at $\sim +265$ mV

in Supplementary Figure 2c. Both DBs can also be made neutral by reducing the sample bias to bring the tip Fermi level below the charge transition levels for both DBs, as shown in Supplementary Figure 3a.

One DB Perturbing a Pair: We next consider the “2+1” experiment with a single negative DB perturbing a pair as shown in Figs. 2j-o of the main text. The $\Delta f(V)$ spectra with added offset are reproduced in Supplementary Figure 2f,i. First, we examine the curves for the perturber and the paired DB furthest from the perturber (orange and dark blue in Supplementary Figure 2e,f, red and teal in Supplementary Figure 2h,i). In all cases the sharp charge transition step is observed at approximately -50 mV. Contrasting this with the charge transition value for a lone DB (-135 mV), it is apparent that an absolute shift of 85 mV occurred. This shift can be explained by the presence of the negative charge at the perturbing DB (for bias values between -50 mV to 395 mV), electrostatically shifting all nearby DB levels. In other words, referencing specifically Supplementary Figure 2f, when a $\Delta f(V)$ spectrum is taken with the tip over the blue DB, the step is at -50 mV because the far orange perturbing DB is negative and shifts the level 85 mV closer to zero. The related qualitative band-bending diagram is depicted in Supplementary Figure 4b (corresponding to region **II** in the reproduced $\Delta f(V)$ spectra at the bottom). When both orange and blue are negative (-50 mV to 395 mV), they cause a potential energy increase for the middle teal DB pushing its DB (0/-) level above the sample Fermi level, leaving it neutral. Hence, when taking a $\Delta f(V)$ spectrum over the teal DB, the tip level must be swept to $\sim +395$ mV before it can cross the teal’s DB (0/-) transition level and capture an additional electron to become negative (Supplementary Figure 4c). As done for the pair, the tip level can also be swept below the charge transition levels for all three (≤ -50 mV) rendering them all neutral (Supplementary Figure 4a).

Symmetrically Perturbed Pair of DBs: We finally consider the “1+2+1” experiment where the two close DBs were symmetrically perturbed by two DBs. The “outside” DBs (red and orange labels, Supplementary Figure 2j-l) show a relatively small shift of 22 mV of the (0/-) charge transition levels, due to the distance of 12 lattice sites between the perturbers. Furthermore, the presence of two negative charges raises the charge transition levels of the inner dots (blue and teal) to +80 mV.

Supplementary Table 1: Truth table of an OR Gate.

OR Gate Input 1	OR Gate Input 2	Output	Figure
0	0	0	4e,f
0	1	1	4h,i
1	0	1	4k,l
1	1	1	4n,o

Sim-Anneal

The sequential OR gates of Supplementary Figure 6 were simulated and output using the Sim-Anneal engine in the Silicon Quantum Atomic Designer software⁵⁹. Each iteration of the gate inputs was run for 10,000 anneal cycles at 4K assuming a Fermi-level $V_0=0.270$ and a Debye Length of 4.3 nm.

Details on Tip-induced Band Bending

During AFM imaging, even at zero applied bias, the tip affects the electrostatic potential and, under certain conditions, the occupation of the DB system. The effect can be linked to the contact potential difference, whose source is the difference between the work functions of the tip and the sample. For a tungsten tip, the work function varies with the crystal orientation and is typically taken to be between 4.5 and 5 eV. For a silicon sample, the work function varies significantly with doping type and level. For n-type Si at low temperature, the work function is close to the electron affinity, typically 4.05 eV, being less than this value for a degenerate sample, and greater for a non-degenerate sample. In our case, for our tungsten tip the work function was assumed to be 4.5 eV, while for the silicon sample, considering the low-temperature and a surface dopant concentration of 10^{18} cm^{-3} , it was estimated at 4.1 eV.

This difference in work functions leads to band-bending locally under the tip apex that can shift the electronic levels of dangling bonds, thereby potentially emptying or filling them. We refer to the shift as tip induced band bending (TIBB). TIBB is strongest immediately under the tip apex.

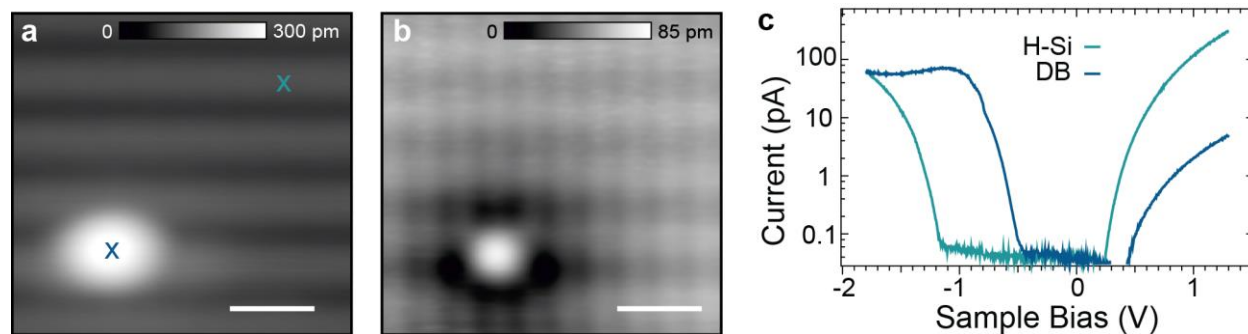
For the above quoted work functions, the TIBB is in the upward direction at zero applied bias voltage, *i.e.*, levels get shifted upward with respect to the sample fermi level $E_{F,\text{sample}}$. While the contact potential difference is a constant, the TIBB changes with both tip-sample separation, as well as applied tip-sample bias (See Supplementary Figure 5). If an electronic level for a DB is shifted above $E_{F,\text{sample}}$, then it cannot stay filled (occupied) in electrochemical equilibrium.

The exact value of TIBB depends not only on the contact potential V_c , but also on the following parameters: sample doping level (N_d), tip-sample bias (V_{st}), tip shape, apex radius (R_t), and the distance (height) between the tip and the surface (d). The TIBB in Supplementary Figure 5 was calculated using our best estimates for the above parameters. A 3D finite-element Poisson equation solver was employed to calculate the TIBB using methodology described in reference ⁷⁰.

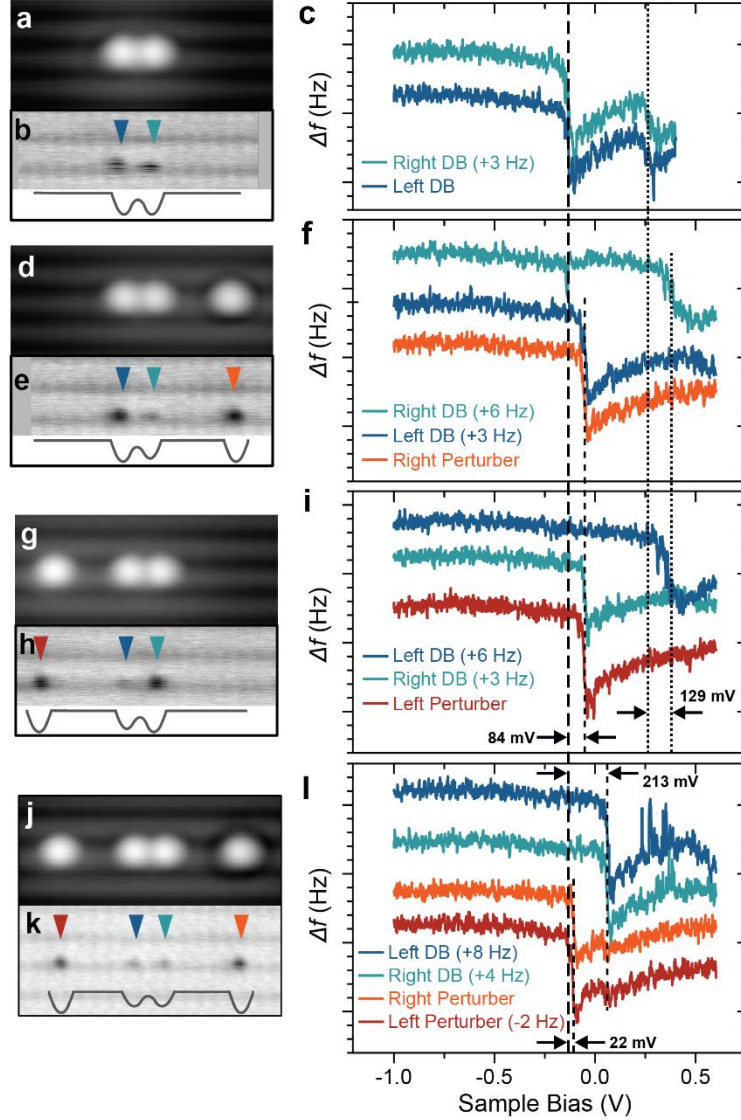
Supplementary References

70. Ryan, P.M., Livadaru, L., DiLabio, G.A. & Wolkow, R.A. Organic nanostructures on hydrogen-terminated silicon report on electric field modulation of dangling bond charge state. *J. Am. Chem. Soc.* **134**, 12054–12063 (2012).

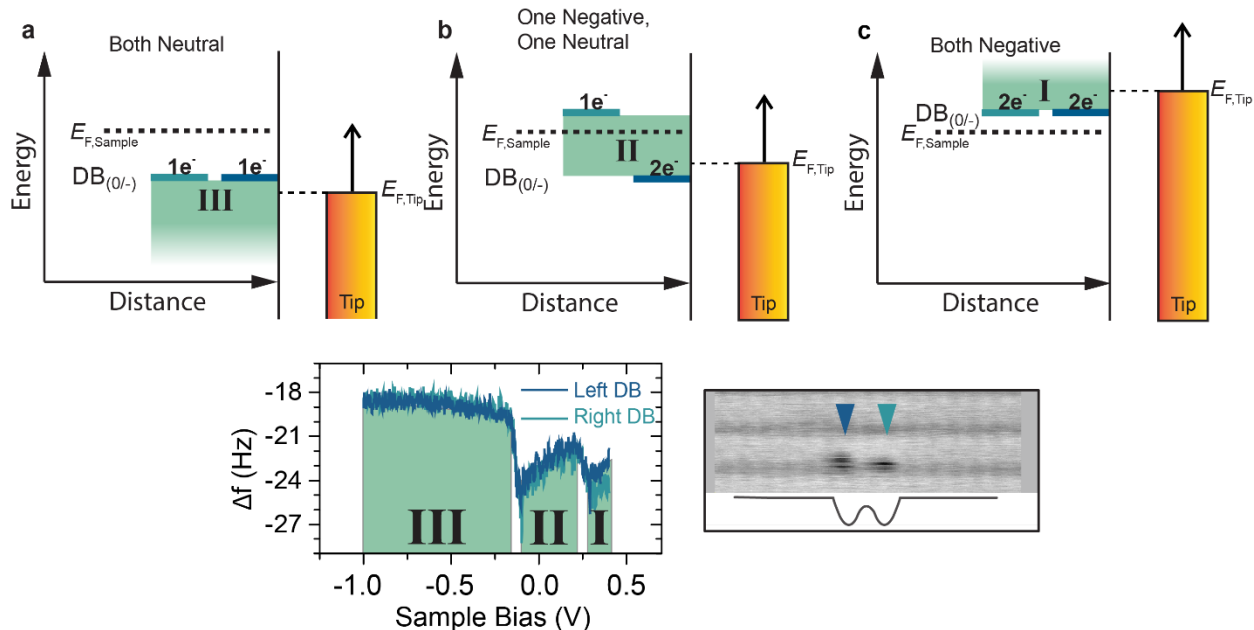
Supplementary Figures



Supplementary Figure 1: STM Characterization of a Dangling Bond. (a) $4 \times 4 \text{ nm}^2$ filled states STM image ($V = -1.8 \text{ V}$, $I = 50 \text{ pA}$) and (b) $4 \times 4 \text{ nm}^2$ empty states STM image ($V = 1.3 \text{ V}$, $I = 50 \text{ pA}$) of a DB. (c) Tunnelling current vs. sample bias ($I(V)$) spectroscopy plotted in log scale of the DB (blue curve) and hydrogen-terminated surface (teal curve). Spectroscopy positions indicated in (a).

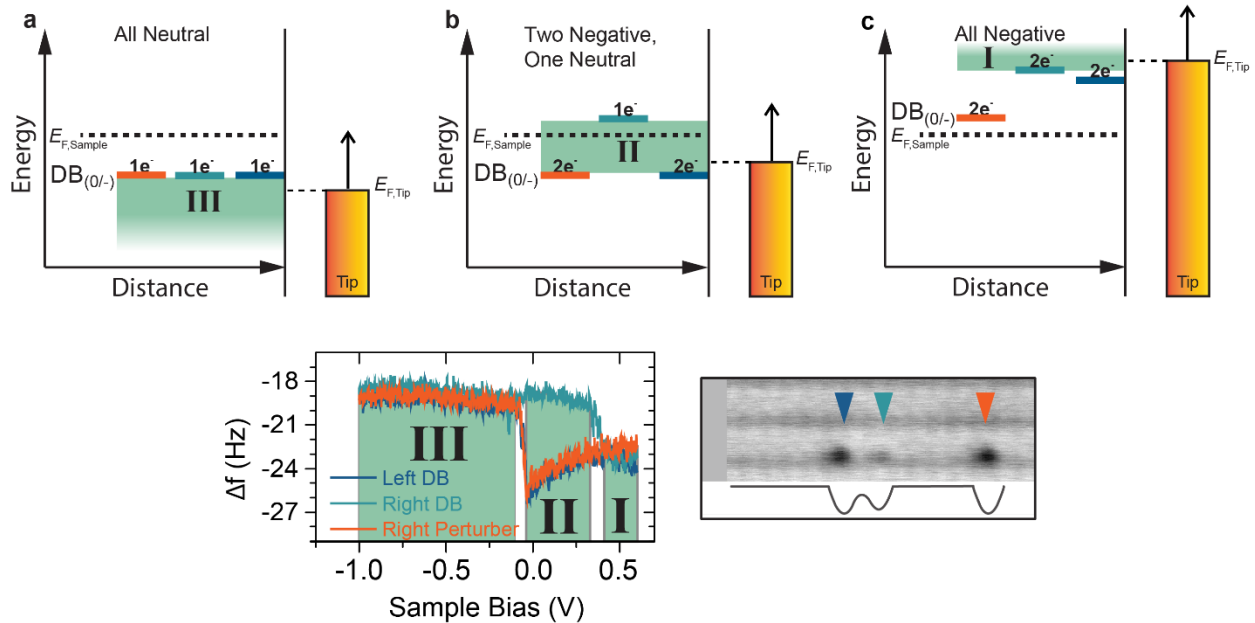


Supplementary Figure 2: Frequency Shift Spectroscopy in Dangling Bond Structures. Colour coded spectra from main text Figure 2 reproduced with vertical offsets for the $\Delta f(V)$ to show key features for the pair (a-c), left tipped (d-f), right tipped (g-i), and symmetric (j-l) cases (being STM, constant-height AFM, and vertically offset $\Delta f(V)$, respectively for each case). The charge transition onset for the isolated DB cases, taken from the pair in (c), is marked with a vertical long-dashed line for reference. A short-dashed line, only in (f) and (i), indicates the shifted charge transition in the presence of one additional charge (the perturber). The finely dotted lines indicate the charge transition onset for bringing in the second charge to the pair (c) as well as for the perturbed dot (f,i) in the presence of the charge of the perturber. In (l), the shifted charge transition onset of the perturbers in the presence of its symmetric perturbing partner is marked by a short-dashed line only running over the orange and red spectra. The transition for bringing in an additional electron for the middle pair is marked by the short-dashed line. STM images in (a),(d),(g), and (j) were taken with $V = -1.8$ V, $I = 50$ pA. The Δf images in (b), (e), (h) and (k) were taken with $z_{\text{rel}} = -300$ pm, and $V = 0$ V. All $\Delta f(V)$, were also taken at $z_{\text{rel}} = -300$ pm (the same as reported in main text Figure 2).

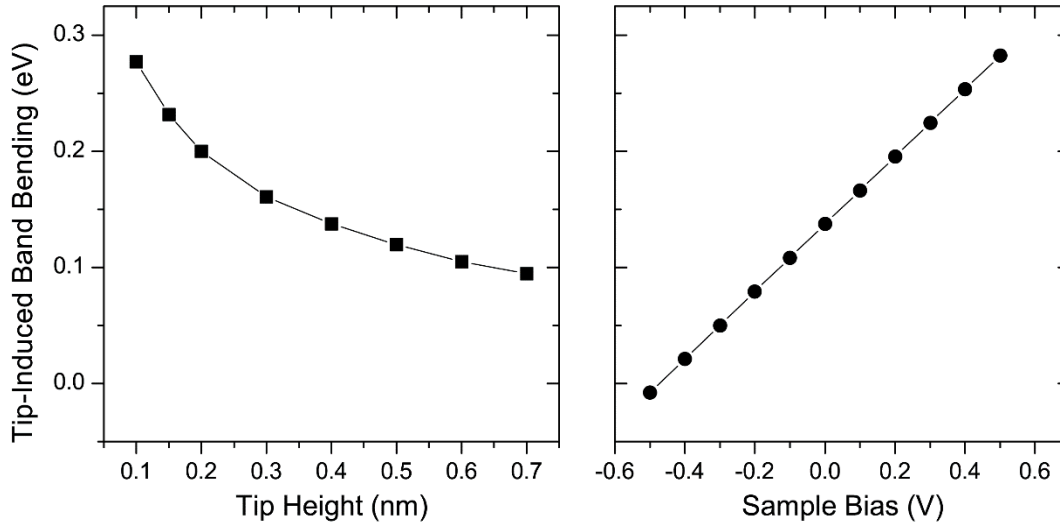


Supplementary Figure 3: Diagrams for Charge Transitions in a Dangling Bond Pair.

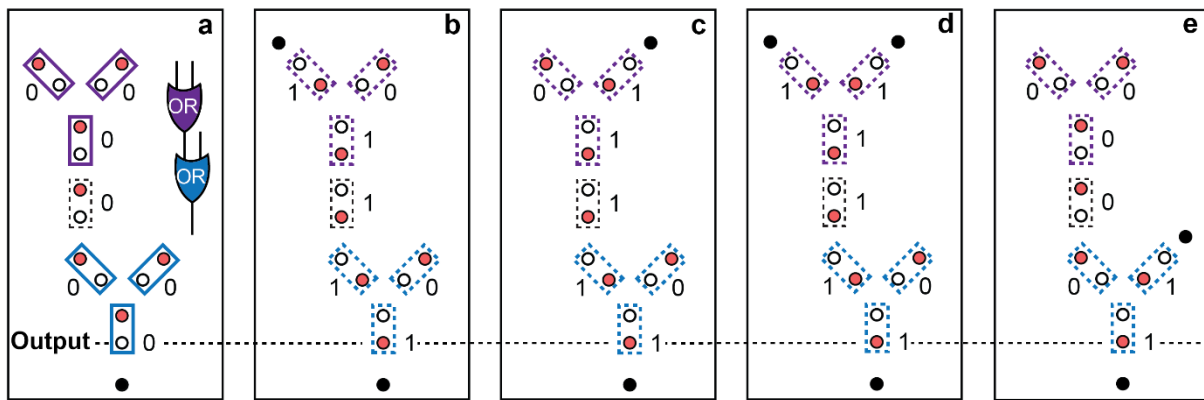
(a) Diagram of the system when both DBs are neutrally charged. The tip is assumed to be positioned above the dark blue DB. The DB's negative to neutral charge transition levels are plotted on the left, and are colour coded to the $\Delta f(V)$ reproduced from main text Figure 2 below. The Fermi level for tip and sample are given by the dotted lines. The tip Fermi level is below both charge transition levels, meaning both are singly occupied. This corresponds to region III for sample bias \leq less than -135 mV. (b) Diagram for the same system when the sample bias is between -135 mV to 265 mV. Only the blue DB is negative. The teal DB is neutral, as its charge transition level has been shifted above the Fermi level of the sample from the negative charge of the blue DB. This corresponds to region II in the $\Delta f(V)$ spectra. (c) Diagram for sample bias values greater than 265 mV (region I) in the $\Delta f(V)$ spectrum of two closely spaced DBs where both are negatively charged. The Fermi level of the tip is now above the negative to neutral charge transition level $DB(0/-)$ of both DBs, rendering them both negative.



Supplementary Figure 4: Diagrams for Charge Transitions in a Biased Pair of Dangling Bonds. (a) Diagram of the system when all DBs are neutrally charged. The DB's negative to neutral charge transition levels $DB(0/-)$ are colour coded to the $\Delta f(V)$ spectrum at the bottom reproduced from main text Fig. 2. The Fermi level for tip and sample are given by the dotted lines. The tip Fermi level is below all charge transition levels, meaning all are singly occupied. This corresponds to region III for bias ≤ -50 mV. (b) The diagrams for the same system when the sample bias is decreased to between -50 mV to 395 mV. The perturbing orange DB and blue DB are both negative, lifting the level for the teal above the Fermi level of the sample and rendering it neutral. This corresponds to region II in the $\Delta f(V)$ spectra. (c) Diagrams for sample bias ≥ 395 mV (region I) in. The Fermi level of the tip is now above charge transition level of all DBs, rendering them all negative.



Supplementary Figure 5: Calculated Tip-Induced Band Bending as a Function of Height and Bias. (a) Tip-induced band bending as a function of tip-sample height. No bias is applied between tip and sample. (b) Tip-induced band bending as a function of sample bias for a fixed tip-sample separation of 0.4 nm. For both plots, we assumed a donor concentration of 10^{18} cm^{-3} at the surface, gradually increasing to $2 \times 10^{19} \text{ cm}^{-3}$ in the bulk over a range of approximately 100 nm, a work function difference between tip and sample of 0.4 eV, and a tip radius of 10 nm.



Supplementary Figure 6: Sequential OR Gates. (a) Two OR gates in sequence (symbols and boxes in solid purple and blue), connected by a binary wire (one bit long in this example; black dashed box). Functionality is shown by adding inputs (black dots = perturber DB representing connections to other pair-based binary structures or anticipated electrical contacts) to the purple gate's upper input branches with (b) (1,0), (c) (0,1), and (d) (1,1). In (e), the input of the lower blue OR gate is toggled to (0,1). In the latter configuration, any further input to the first gate would not change the output state from '1'.